Extended lattice Boltzmann scheme for droplet combustion

Mostafa Ashna,[1] Mohammad Hassan Rahimian,[1] and Abbas Fakhari[2]

[1]*School of Mechanical Engineering, College of Engineering, University of Tehran, Tehran, Iran*

[2]*Department of Civil and Environmental Engineering and Earth Sciences, University of Notre Dame, Notre Dame, Indiana 46556, USA*

The available lattice Boltzmann (LB) models for combustion or phase change are focused on either single-phase flow combustion or two-phase flow with evaporation assuming a constant density for both liquid and gas phases. To pave the way towards simulation of spray combustion, we propose a two-phase LB method for modeling combustion of liquid fuel droplets. We develop an LB scheme to model phase change and combustion by taking into account the density variation in the gas phase and accounting for the chemical reaction based on the Cahn-Hilliard free-energy approach. Evaporation of liquid fuel is modeled by adding a source term, which is due to the divergence of the velocity field being nontrivial, in the continuity equation. The low-Mach-number approximation in the governing Navier-Stokes and energy equations is used to incorporate source terms due to heat release from chemical reactions, density variation, and nonluminous radiative heat loss. Additionally, the conservation equation for chemical species is formulated by including a source term due to chemical reaction. To validate the model, we consider the combustion of n-heptane and n-butanol droplets in stagnant air using overall single-step reactions. The diameter history and flame standoff ratio obtained from the proposed LB method are found to be in good agreement with available numerical and experimental data. The present LB scheme is believed to be a promising approach for modeling spray combustion.

I. INTRODUCTION

Liquid fuels account for over 30% of the world's energy consumption [1]. They could be combusted in internal combustion engines, gas turbines, rockets, industrial furnaces, steam generators, and other combustive devices [2]. Liquid fuels are usually sprayed into individual droplets that are dispersed in a gas phase to facilitate combustion. Detailed study of the combustion mechanism of these individual droplets is vital for understanding spray combustion, which is of fundamental importance in improving the efficiency of combustion in general and producing fewer emissions in particular [3].

Early theoretical studies on droplet combustion and its observation by experimentalists in the 1950s are reviewed by Law [4]. In early theoretical studies, numerous assumptions were made, such as a quasisteady process, symmetric droplet, and quiescent environment. Based on these assumptions, Godsave [5] presented the first theoretical model of evaporation and combustion of fuel droplets, and attained the so-called d^2 law, which indicates that the square of the droplet diameter decreases linearly with time. Theoretical studies in the next three decades were limited in structure, objective, and vision because of the nonlinearity of the Navier-Stokes equations [6,7]. Therefore, numerical and analytical solutions were developed for more realistic conditions by including additional physical complications [6].

Experiments have shown that while the gasification rate is constant after ignition, the flame standoff ratio (FSR) is unsteady [8]. Incorporating unsteadiness into numerical simulations is quite complicated and costly [6,9]. Ulzama and Specht [8] proposed an analytical model for unsteady droplet combustion in spherical coordinates by assuming that the diffusion process occurring in between the exterior surface of the droplet and the engulfing flame is quasisteady, while the diffusion process elsewhere is unsteady. The variations in droplet diameter, FSR, and gasification rate obtained by this

approach were found to be in agreement with experimental data [8]. Tyurenkova [10] developed an analytical model for nonequilibrium phase transition of droplet combustion. He concluded that when the droplet radius tends to zero the equilibrium assumption for phase change leads to erroneous results such as underestimation of burning time. Wu and Sirignano [11] numerically investigated the transient combustion of n-octane in a hot gas flow. They considered the effects of many factors such as reduction in droplet size, reduction of flow velocity due to drag, vortical flow inside the droplet, variable thermophysical properties, nonuniform temperature distribution at the surface of the droplet, and surface tension. They modeled combustion using a single infinitely fast reaction and considered self-ignition and flame shape history in their simulations. Later on, Farouk *et al.* [12] conducted both experiments and numerical simulations to account for detailed chemical kinetics, variable physical properties, and radiative heat transfer. They used the transient conductive model to numerically simulate heat transfer inside the droplet. They also measured the diameter, FSR, and burning rate of a methyl butanoate droplet in microgravity conditions, experimentally.

Another comprehensive simulation was conducted by Awasthi *et al.* [13]. They investigated the effects of droplet size for isolated methanol drops in high-temperature and nearly quiescent ambient air. Their results show that droplet size has a significant effect on the combustion regime, which transforms from a kinetically controlled regime in small droplets to a diffusion-controlled regime in larger droplets. In smaller droplets, the flame-sheet approximation is not valid and the flame has a large reactive zone [13]. Therefore, using only one overall reaction with flame-sheet approximation restricts their numerical solutions to large droplets. In another study [14], they extended their simulations to n-heptane droplets and investigated the effects of ambient temperature and droplet size. They also studied the ignition delay time, flame temperature, FSR, and heat release. Recently, Alam *et al.* [15]

numerically analyzed droplet combustion by considering the detailed gas-phase chemical kinetics, radiative heat transfer, multicomponent diffusive transport, and variable physical properties. They modeled combustion using both large-order and reduced-order kinetic mechanisms. In addition to numerical simulations, they conducted experiments to measure the main parameters in combustion, such as droplet size history, FSR, and burning rate of submillimeter n-butanol droplets.

In all of the above-mentioned numerical investigations, the conventional computational fluid dynamics (CFD) methods are used to solve the Navier-Stokes equations. Alternatively, the lattice Boltzmann method (LBM) has become an established numerical technique for simulation of fluid flow problems, particularly for two-phase flows and microscale phenomena [16,17]. Thanks to its mesoscopic nature, LBM has proven to be a competitive method for simulation of multiscale multiphase flows [18,19], including the microscale droplet evaporation and phase change [20–23], which is the focus of the present study. Simulation of the microscale reaction has also been considered by Ayodele et al. [24]. They studied pattern formation in reaction-diffusion systems for a single species using LBM.

Succi et al. [25] simulated a coflowing methane-air laminar flame using LBM. They used the 24-speed face-centered-hypercubic (FCHC) LB scheme with two sets of distribution functions: one for the density and velocity, and one for the mixture fraction. The main shortcoming of their model is that the density was not coupled with the temperature variation due to reaction heat release; therefore their results did not agree with available experimental or numerical data.

In low-speed reactive flows, where sound waves do not have a significant effect on combustion, the main characteristic of the flow field is a small Mach number such that density variation is only due to temperature and composition variations [26]. In order to couple density and temperature variations, Filippova and Hanel [27–29] introduced the low-Mach-number approximation (LMNA) of the Navier-Stokes equations for modeling combustion using LBM. They proposed a hybrid LBM and finite-difference method to solve the flow field using an LB scheme while using finite differences to solve for the temperature and chemical species. Yamamoto et al. [30] introduced an LB scheme to solve for pressure, temperature, and chemical species concentration fields. In their method, the density was considered to be constant without any relation to temperature and chemical composition. In another study [31], they modeled a counterflow diffusion flame using both a single-step reaction and a detailed kinetic mechanism. Although they considered detailed chemistry mechanisms, their results were not entirely realistic because the density was assumed to be constant. Lee et al. [32] proposed a new LBM for simulation of laminar diffusion flames with a variable density. They assumed the LMNA in the momentum equation for recovering the velocity and hydrodynamic pressure alongside the mixture fraction, which determined the temperature and chemical species in the flow field. The thermodynamic pressure was assumed to be constant and the density variation was coupled to temperature and concentration variations through the ideal gas equation of state. Chen et al. [33,34] proposed an LBM for combustion that determined the temperature and chemical species separately. They modified the relaxation time

and viscosity as a function of a characteristic temperature in every time step. The density was evaluated through the equation of state by assuming a constant thermodynamic pressure. They claimed that their model led to better numerical results compared with other LB models.

Despite all the advantages of LBM in simulating a two-phase combustion problem, the published literature is devoted to single-phase flow combustion, and no mathematical model is available for multiphase flow combustion using LBM. This involves the modeling evaporation phase change and chemical reaction, both of which are of crucial importance in droplet combustion. In our previous study by Safari et al. [20], we proposed an extended LB scheme based on an advanced free-energy model [35] for simulation of evaporation and phase-change mechanisms. This was achieved by incorporating a proper source term in the convective Cahn-Hilliard equation. This source term accounted for the fact that the divergence of velocity is not zero at the interface because of the bulk motion of the vapor into the gas phase during phase change. The LB method introduced in Ref. [20] is used for simulation of early stages of boiling (nucleation) and bubble release from a liquid pool with constant temperature [22] and with variable temperature in the liquid phase [23], and for simulation of droplet evaporation on hot porous surfaces [36] as well as vapor condensation, liquid film formation, and dew drop sprinkling [37]. Although the phase-change model is the same in all of the aforementioned studies [22,23,36,37], the physical phenomena and boundary conditions are different. Another similarity in the above-mentioned papers is that the gas density is assumed to be constant while it should be a function of the temperature in open systems.

In this study, we extend the original formulation by Safari et al. [20] to include additional terms to account for variations in the gas density, in the continuity equation. Since the combustion causes significant variation in the temperature, the variable gas density approach is essential for accurate modeling of combustion phenomena. The LMNA is used to account for a variable density in the mesoscopic LB formulations. The combustion is incorporated into the model by employing a new distribution function for chemical species with the reaction source term. The temperature variation causes a change in the fluid properties, including the density, diffusivity, and speed of sound. The lattice speed in the gas phase and the corresponding relaxation time are modified to account for these variations. To verify the proposed model, the combustion of an isolated fuel droplet surrounded by air is simulated and the results are compared with experimental and numerical data where available. Although our scheme has no limitation in terms of Prandtl number, which is the ratio of viscous diffusivity to thermal diffusivity, and Lewis number, which is the ratio of thermal diffusivity to mass diffusivity, it does not include the autoignition, ignition, and extinction phenomena yet.

II. MATHEMATICAL MODELING

A. Macroscopic equations

We focus on combustion at low Mach numbers as a simple but practical case. The governing macroscopic equations are

the conservation of mass, momentum, energy, and chemical species, as well as an equation of state for determining the local gas density. Additionally, the Cahn-Hilliard equation [20,35] is used to track the interface between liquid and gas phases. The LMNA is applied to the Navier-Stokes equation, energy equation, and mass fraction of species [26–29]. With the LMNA, the pressure in the momentum equation is divided into two parts, thermodynamic pressure P_{th} and hydrodynamic pressure P_h. In steady (or quasisteady) flow, which is the main assumption in modeling droplet combustion, the change in the pressure is proportional to $O(\mathrm{Ma}^2)$. In unsteady combustive flows, the change in the pressure is proportional to $O(\mathrm{Ma})$. Thus, for subsonic combustion, the pressure variation is negligible and the thermodynamic pressure can be assumed constant in the equation of state $P_{th} = \rho R_u / \bar{W} T =$ const., and its spatial and temporal derivatives are zero [33]. Therefore, the density is a function of temperature and mean molecular weight, which is a function of the chemical composition. Other assumptions are as follows:

(1) The only body force is the surface tension force that is acting at the interface.

(2) The temperature of the droplet is a constant value below the boiling point. In addition, the mass fraction of the fuel inside the droplet is equal to 1 [4]. These two assumptions lead to a constant density in the liquid phase.

(3) The droplet is stationary and there is no vortical flow inside the droplet.

(4) The chemical reaction of combustion is the only heat source, and the nonluminous radiation of hot gases (CO_2 and H_2O) is modeled as the only mechanism for heat dissipation.

(5) The density of the gas phase, which is assumed to be a mixture of ideal gases [33], is a function of temperature and chemical composition according to an ideal gas equation of state.

Therefore, the resulting equations are

$$\frac{\partial \rho}{\partial t} + \frac{\partial \rho u_i}{\partial x_i} = 0, \tag{1}$$

$$\frac{\partial \rho u_i}{\partial t} + \frac{\partial \rho u_i u_j}{\partial x_j} = -\frac{\partial P_h}{\partial x_i} + \frac{\partial}{\partial x_j}\left[\mu\left(\frac{\partial u_i}{\partial x_j} + \frac{\partial u_j}{\partial x_i}\right)\right] + F_i, \tag{2}$$

$$\frac{\partial T}{\partial t} + u_i \frac{\partial T}{\partial x_i} = \frac{1}{\rho c_p}\frac{\partial}{\partial x_i}\left(k\frac{\partial T}{\partial x_i}\right) + \frac{1}{\rho c_p}\left(\sum_{z=1}^{N} h_z \omega_z - \dot{Q}_R\right), \tag{3}$$

$$\frac{\partial Y_z}{\partial t} + u_i \frac{\partial Y_z}{\partial x_i} = \frac{1}{\rho}\frac{\partial}{\partial x_i}\left(D_z \rho \frac{\partial Y_z}{\partial x_i}\right) + \frac{1}{\rho}\omega_z$$
$$z = 1, \dots, N-1, \left(\sum_{z=1}^{N} Y_z = 1\right), \tag{4}$$

$$\rho_g = \frac{P_{th}\bar{W}}{R_u T} = \frac{P_{th}}{R_u T \sum \frac{Y_z}{W_z}}, \tag{5}$$

where ρ is the local averaged density; ρ_g is the bulk density of the gas phase; u_i is the velocity vector component; μ is the dynamic viscosity; F_i is the body force; c_p is the specific heat capacity; k is the thermal conductivity; T is the temperature; Y_z, D_z, and h_z are the mass fraction, diffusion coefficient, and enthalpy of formation of species z, respectively; R_u is the universal gas constant; $\bar{W}$ is the mean molecular weight of gas; and W_z is the molecular weight of species z. Since most of the air's chemical composition is nitrogen, the diffusion coefficient of the species relative to nitrogen is used. $\dot{Q}_R = 4\kappa_p \sigma T^4$ is the heat loss due to nonluminous radiation (from H_2O and CO_2) [13,38], in which $\sigma = 5.67 \times 10^8\,\mathrm{W/m^2\,K}$ is the Stefan-Boltzmann constant and κ_p is the mean Planck absorption coefficient [38]. The production or consumption rate of the chemical species ω_z is obtained from the single-step overall reaction rate ω_{ov} as

$$\omega_z = \omega_{ov} a_z W_z, \tag{6}$$

with

$$\omega_{ov} = K_{ov}\rho^2 \frac{Y_{\text{fuel}}}{W_{\text{fuel}}} \frac{Y_{ox}}{W_{ox}} \exp\left(-\frac{E}{R_u T}\right), \tag{7}$$

where a_z is the stoichiometric coefficient, which is negative for the reactants and positive for the products; K_{ov} is the reaction coefficient; E is the effective activation energy; Y_{fuel} and Y_{ox} are the mass fraction of fuel and oxygen, respectively; and W_{fuel} and W_{ox} are the molecular weight of fuel and oxygen, respectively. The chemical species mass fraction equation (4) is solved for all the chemical species except for nitrogen, which does not participate in chemical reaction. The mass fraction of nitrogen is simply computed by $\sum_{z=1}^{N} Y_z = 1$.

B. Extended Cahn-Hilliard equation

Following Safari *et al.* [20], different fluid phases (liquid and gas) are determined via the order parameter $C = \frac{\tilde{\rho}_l}{\rho_l} = 1 - \frac{\tilde{\rho}_g}{\rho_g}$, $(0 \leqslant C \leqslant 1)$, where $\tilde{\rho}_l$ and $\tilde{\rho}_g$ are the local densities of the liquid and gas phases, respectively, and ρ_l is the bulk density of the liquid phase. The local averaged density is calculated by

$$\rho = \tilde{\rho}_l + \tilde{\rho}_g = C\rho_l + (1-C)\rho_g. \tag{8}$$

The continuity equation for each phase includes a source term [20],

$$\frac{\partial \tilde{\rho}_\zeta}{\partial t} + \frac{\partial n_{i\zeta}}{\partial x_i} = \pm \dot{m}''', \tag{9}$$

where $\dot{m}'''$ is the source term due to evaporation that is positive for the gas phase and negative for the liquid phase, $n_{i\zeta}$ is the mass flux for each phase, and $\zeta \in l,g$ stands for either liquid or gas. Note that in the chemical reaction that occurs in the gas phase, although the mixture chemical composition changes, the total mass is conserved. Therefore, the only source term is that due to evaporation. The mass flux in each phase can be written in terms of the density and diffusive flow rate $J_{i\zeta}$ as [39]

$$n_{i\zeta} = \tilde{\rho}_\zeta u_i - \rho_\zeta J_{i\zeta}. \tag{10}$$

Using Eq. (10) and the definition of the order parameter, Eq. (9) can be rewritten as

$$\frac{\partial C}{\partial t} + \frac{\partial (u_i C)}{\partial x_i} - \frac{\partial J_{il}}{\partial x_i} = -\frac{\dot{m}'''}{\rho_l} \qquad (11)$$

for the liquid phase and

$$\frac{\partial (1-C)}{\partial t} + \frac{\partial ((1-C)u_i)}{\partial x_i} - \frac{\partial J_{ig}}{\partial x_i} + \frac{1}{\rho_g}$$
$$\times \left[(1-C)\left(\frac{\partial \rho_g}{\partial t} + u_i \frac{\partial \rho_g}{\partial x_i} \right) - J_{ig} \frac{\partial \rho_g}{\partial x_i} \right] = \frac{\dot{m}'''}{\rho_g} \qquad (12)$$

for the gas phase. The terms in the brackets account for the variation in the gas density due to variations in temperature and composition. If the diffusive flow rate is only due to the difference in composition, then $J_l = -J_g = J$ [39]. Cahn and Hilliard [35] assumed that the diffusive flow rate is a function of the chemical potential, say, $J_i = M \partial \mu_C / \partial x_i$, in which $M > 0$ is the mobility and μ_C is the chemical potential. Using the mixing energy concept, they related the chemical potential to the order parameter by $\mu_C = \mu_{C0} - \kappa \partial^2 C / \partial x_i^2$, in which $\mu_{C0} = \frac{\partial}{\partial C}[\beta C^2(1-C^2)]$ is the classical part of the chemical potential, and β and κ are related to the interface thickness ϵ and surface tension σ by $\beta = \frac{12\sigma}{\epsilon}$ and $k = \frac{3\sigma\epsilon}{2}$ [35]. Equation (11) can be rewritten in terms of the chemical potential as

$$\frac{\partial C}{\partial t} + \frac{\partial (u_i C)}{\partial x_i} = \frac{\partial}{\partial x_i}\left(M \frac{\partial \mu_C}{\partial x_i} \right) - \frac{\dot{m}'''}{\rho_l}. \qquad (13)$$

Equation (13) is the extended Cahn-Hilliard equation for phase change, which will be solved using the LBM proposed in Sec. III B. Adding Eqs. (11) and (12) yields

$$\frac{\partial u_i}{\partial x_i} = \dot{m}'''\left(\frac{1}{\rho_g} - \frac{1}{\rho_l} \right)$$
$$- \frac{1}{\rho_g}\left[(1-C)\left(\frac{\partial \rho_g}{\partial t} + u_i \frac{\partial \rho_g}{\partial x_i} \right) + J_i \frac{\partial \rho_g}{\partial x_i} \right], \qquad (14)$$

which shows that the divergence of the velocity is related to the evaporation and density variation. The source term due to evaporation exists only in the interface while the term due to density variation is considerable in the reaction zone.

III. LATTICE BOLTZMANN MODELING

A. Lattice Boltzmann equation for momentum

The following discrete Boltzmann equation has been previously proposed to model phase change in a two-phase system [20]:

$$\frac{Dg_\alpha}{Dt} = -\frac{1}{\lambda}\left(g_\alpha - g_\alpha^{eq} \right) + (e_{\alpha i} - u_i)\,\Psi_{\alpha,i} + \rho c_s^2 \frac{\partial u_i}{\partial x_i}\xi_\alpha, \quad (15)$$

where g_α is the hydrodynamic distribution function, t is time, λ is the relaxation time, $e_{\alpha i}$ is the lattice velocity set, ξ_α is the weight coefficient set, and $c_s = c/\sqrt{3}$ is the speed of sound with c being the lattice speed. Additionally,

$$g_\alpha^{eq} = P_h \xi_\alpha + \rho c_s^2 (\Gamma_\alpha - \xi_\alpha), \qquad (16)$$

and the auxiliary variables are

$$\Gamma_\alpha = \xi_\alpha\left[1 + \frac{e_{\alpha i} u_i}{c_s^2} + \frac{(e_{\alpha i} e_{\alpha j} - c_s^2 \delta_{ij})u_i u_j}{2c_s^4} \right], \qquad (17)$$

and

$$\Psi_{\alpha,i} = \left[\frac{\partial \rho c_s^2}{\partial x_i}(\Gamma_\alpha - \xi_\alpha) - C \frac{\partial \mu_C}{\partial x_i}\Gamma_\alpha \right], \qquad (18)$$

where $-C\frac{\partial \mu_C}{\partial x_i}$ is the interfacial tension force [20]. As mentioned before, in the LMNA of fluid flow in open systems it is assumed that the thermodynamic pressure is constant [26]. Using the ideal gas equation of state for the gas phase and considering a constant thermodynamic pressure, the temporal and spatial derivatives of ρ_g become

$$\frac{\partial \rho_g}{\partial t} = -\frac{P_{th}}{R_u} \frac{1}{T^2\left(\sum \frac{Y_z}{W_z} \right)^2}\left(\frac{\partial T}{\partial t}\sum \frac{Y_z}{W_z} + T\frac{\partial}{\partial t}\sum \frac{Y_z}{W_z} \right),$$
$$\qquad (19)$$

$$\frac{\partial \rho_g}{\partial x_i} = -\frac{P_{th}}{R_u} \frac{1}{T^2\left(\sum \frac{Y_z}{W_z} \right)^2}\left(\frac{\partial T}{\partial x_i}\sum \frac{Y_z}{W_z} + T\frac{\partial}{\partial x_i}\sum \frac{Y_z}{W_z} \right).$$
$$\qquad (20)$$

Substituting Eqs. (19) and (20) into Eq. (14) yields

$$\frac{\partial u_i}{\partial x_i} = \dot{m}'''\left(\frac{1}{\rho_g} - \frac{1}{\rho_l} \right) + \Omega, \qquad (21)$$

where the auxiliary variable

$$\Omega = \frac{P_{th}}{\rho_g R_u}\frac{1}{T^2\left(\sum \frac{Y_z}{W_z} \right)^2}\left\{ (1-C)\left[\left(\frac{\partial T}{\partial t}\sum \frac{Y_z}{W_z} + T\frac{\partial}{\partial t}\sum \frac{Y_z}{W_z} \right) + u_i\left(\frac{\partial T}{\partial x_i}\sum \frac{Y_z}{W_z} + T\frac{\partial}{\partial x_i}\sum \frac{Y_z}{W_z} \right) \right] \right.$$
$$\left. + M\frac{\partial \mu_C}{\partial x_i}\left(\frac{\partial T}{\partial x_i}\sum \frac{Y_z}{W_z} + T\frac{\partial}{\partial x_i}\sum \frac{Y_z}{W_z} \right) \right\}$$
$$\qquad (22)$$

is the volumetric source that accounts for the density variation due to changes in temperature or chemical composition. Substituting Eq. (21) in Eq. (15) gives

$$\frac{Dg_\alpha}{Dt} = -\frac{1}{\lambda}\left(g_\alpha - g_\alpha^{eq} \right) + (e_{\alpha i} - u_i)\Psi_{\alpha,i} + \xi_\alpha c_s^2\left[\rho\Omega + \rho\dot{m}'''\left(\frac{1}{\rho_g} - \frac{1}{\rho_l} \right) \right], \qquad (23)$$

which can be shown to recover Eq. (2) and the following equation:

$$\frac{1}{\rho c_s^2}\frac{\partial P_h}{\partial t} + \frac{\partial u_i}{\partial x_i} = \dot{m}'''\left(\frac{1}{\rho_g} - \frac{1}{\rho_l}\right) + \Omega. \tag{24}$$

Since the thermodynamic pressure is assumed to be constant [26], $\frac{\partial P_h}{\partial t}$ in Eq. (24) becomes of the order of the truncation error [29] and Eq. (24) reduces to Eq. (14). Applying a trapezoidal integration along characteristics over time step δt leads to the following equation:

$$g_\alpha(x_i + e_{\alpha i}\delta t, t + \delta t) - g_\alpha(x_i, t)$$
$$= -\frac{\delta t}{2\lambda}\left(g_\alpha - g_\alpha^{eq}\right)\Big|_{(x_i + e_{\alpha i}\delta t, t+\delta t)} - \frac{\delta t}{2\lambda}\left(g_\alpha - g_\alpha^{eq}\right)\Big|_{(x_i,t)} + \frac{\delta t}{2}(e_{\alpha i} - u_i)\Psi_{\alpha,i}\Big|_{(x_i + e_{\alpha i}\delta t, t+\delta t)}$$
$$+ \frac{\delta t}{2}(e_{\alpha i} - u_i)\Psi_{\alpha,i}\Big|_{(x_i,t)} + \frac{\delta t}{2}\rho c_s^2\left[\Omega + \dot{m}'''\left(\frac{1}{\rho_g} - \frac{1}{\rho_l}\right)\right]\xi_\alpha\Big|_{(x_i,t)} + \frac{\delta t}{2}\rho c_s^2\left[\Omega + \dot{m}'''\left(\frac{1}{\rho_g} - \frac{1}{\rho_l}\right)\right]\xi_\alpha\Big|_{(x_i + e_{\alpha i}\delta t, t+\delta t)}. \tag{25}$$

To retain a second-order explicit scheme, the following change of variable is made:

$$\bar{g}_\alpha = g_\alpha + \frac{g_\alpha - g_\alpha^{eq}}{2\tau} - \frac{\delta t}{2}(e_{\alpha i} - u_i)\Psi_{\alpha,i} - \frac{\delta t}{2}\rho c_s^2\xi_\alpha\left[\Omega + \dot{m}'''\left(\frac{1}{\rho_g} - \frac{1}{\rho_l}\right)\right], \tag{26}$$

and the modified equilibrium distribution function would be

$$\bar{g}_\alpha^{eq} = g_\alpha^{eq} - \frac{\delta t}{2}(e_{\alpha i} - u_i)\Psi_{\alpha,i} - \frac{\delta t}{2}\rho c_s^2\xi_\alpha\left[\Omega + \dot{m}'''\left(\frac{1}{\rho_g} - \frac{1}{\rho_l}\right)\right]. \tag{27}$$

Substituting Eqs. (26) and (27) into Eq. (25) gives

$$\bar{g}_\alpha(x_i + e_{\alpha i}\delta t, t + \delta t) = \bar{g}_\alpha(x_i, t) - \frac{\bar{g}_\alpha - \bar{g}_\alpha^{eq}}{\tau + 0.5}\Big|_{(x_i,t)} + \delta t(e_{\alpha i} - u_i)\Psi_{\alpha,i}\Big|_{(x_i,t)} + \delta t\rho c_s^2\xi_\alpha\left[\Omega + \dot{m}'''\left(\frac{1}{\rho_g} - \frac{1}{\rho_l}\right)\right]_{(x_i,t)}, \tag{28}$$

where the dimensionless relaxation time $\tau = \lambda/\delta t$ is related to the kinematic viscosity by $\nu = \tau c_s^2\delta t$.

B. Boltzmann equation for interface tracking

While Eq. (28) solves for the velocity and hydrodynamic pressure fields, one needs another equation for identifying each phase according to Eq. (13). As such, the following equation has been proposed [20]:

$$\frac{Dh_\alpha}{Dt} = -\frac{1}{\lambda}\left(h_\alpha - h_\alpha^{eq}\right) + \Pi_i\Gamma_\alpha + \left[\frac{\partial}{\partial x_i}\left(M\frac{\partial\mu_C}{\partial x_i}\right) - \frac{\dot{m}'''}{\rho_l}\right]\Gamma_\alpha, \tag{29}$$

where

$$\Pi_i = (e_{\alpha i} - u_i)\left[\frac{\partial C}{\partial x_i} - \frac{C}{\rho c_s^2}\left(\frac{\partial P_h}{\partial x_i} + C\frac{\partial\mu_C}{\partial x_i}\right)\right], \tag{30}$$

and the equilibrium distribution function for interface tracking is

$$h_\alpha^{eq} = C\Gamma_\alpha. \tag{31}$$

Again, the following change of variable is made to obtain an explicit scheme with a second-order accuracy:

$$\bar{h}_\alpha = h_\alpha + \frac{h_\alpha - h_\alpha^{eq}}{2\tau} - \frac{\delta t}{2}\Pi_i - \frac{\delta t}{2}\Gamma_\alpha\left[-\frac{\dot{m}'''}{\rho_l}\right], \tag{32}$$

where the modified equilibrium distribution function for interface tracking reads

$$\bar{h}_\alpha^{eq} = h_\alpha^{eq} - \frac{\delta t}{2}\Pi_i - \frac{\delta t}{2}\Gamma_\alpha\left[-\frac{\dot{m}'''}{\rho_l}\right]. \tag{33}$$

Applying the trapezoidal integration along characteristics over time step δt results in the following equation:

$$\bar{h}_\alpha(x_i + e_{\alpha i}\delta t, t + \delta t)$$
$$= \bar{h}_\alpha(x_i, t) - \frac{\bar{h}_\alpha - \bar{h}_\alpha^{eq}}{\tau + 0.5}\Big|_{(x_i,t)} + \delta t\Pi_i\Gamma_\alpha\Big|_{(x_i,t)}$$
$$+ \delta t\Gamma_\alpha\left[-\frac{\dot{m}'''}{\rho_l}\right]_{(x_i,t)} + \frac{\delta t}{2}\Gamma_\alpha\left[\frac{\partial}{\partial x_i}\left(M\frac{\partial\mu_C}{\partial x_i}\right)\right]_{(x_i,t)}$$
$$+ \frac{\delta t}{2}\Gamma_\alpha\left[\frac{\partial}{\partial x_i}\left(M\frac{\partial\mu_C}{\partial x_i}\right)\right]_{(x_i + e_{\alpha i}\delta t, t)}. \tag{34}$$

The gradient terms in Eqs. (26)–(28) and (32)–(34) are discretized in the same way as suggested by Lee and Liu [40]. The last term in Eq. (34) is evaluated at $(x_i + e_{\alpha i}\delta t, t)$ instead of $(x_i + e_{\alpha i}\delta t, t + \delta t)$ to maintain an explicit scheme. The dimensionless relaxation time, for both hydrodynamics and interface tracking, is a linear function of the order parameter, $\tau = C\tau_l + (1 - C)\tau_g$, in which $\tau_l = 0.05$ is constant and $\tau_g = \nu_g/c_s^2\delta t$ is a function of the kinematic viscosity and time step. He *et al.* [41] assumed that the lattice speed is related to the average temperature by $c/c_0 = \sqrt{T_{av}/T_0}$, in which c_0 and T_0 are the initial lattice speed and temperature, respectively (please note the difference between the lattice speed c and the order parameter C). Another assumption is that the lattice speed is proportional to $\sqrt{T_{max}}$, in which T_{max} is the maximum temperature in the system [33,34]. In the present study, we also assume $c/c_0 = \sqrt{T_{av}/T_0}$ and adjust δt such that $\delta x = c\delta t = 1$ *lu* (*lu* = lattice unit). This approach leads to an identical speed of sound c_s, which is

modified in every time step, in the entire domain. We assume that the dynamic viscosity of the gas phase is related to the temperature by $\mu_g/\mu_{g0} = \sqrt{T/T_0}$. Therefore, the kinematic viscosity of the gas phase is related to the temperature by $v_g/v_{g0} = (\rho_0/\rho)\sqrt{T/T_0}$, in which v_{g0} and ρ_0 are the initial kinematic viscosity and density, respectively. The initial value of τ_g is determined by $\tau_g/\tau_l = v_g/v_l$.

The order parameter, velocity, and hydrodynamic pressure are calculated by

$$C = \sum_\alpha \bar{h}_\alpha + \frac{\delta t}{2}\left[-\frac{\dot{m}'''}{\rho_l}\right], \tag{35}$$

$$\rho u_i = \frac{1}{c_s^2}\sum_\alpha e_{i\alpha}\bar{g}_\alpha - \frac{\delta t}{2}C\frac{\partial \mu_C}{\partial x_i}, \tag{36}$$

$$P_h = \sum_\alpha \bar{g}_\alpha + \frac{\delta t}{2}u_i\frac{\partial \rho c_s^2}{\partial x_i} + \frac{\delta t}{2}\rho c_s^2\left[\Omega + \dot{m}'''\left(\frac{1}{\rho_g} - \frac{1}{\rho_l}\right)\right]. \tag{37}$$

C. Lattice Boltzmann equation for the temperature

The Boltzmann equation and its equilibrium distribution function for the energy equation can be written as [33]

$$\frac{DE_\alpha}{Dt} = \frac{\partial E_\alpha}{\partial t} + e_{\alpha i}\frac{\partial E_\alpha}{\partial x_i} = -\frac{1}{\lambda_T}\left(E_\alpha - E_\alpha^{eq}\right) + \dot{\gamma}_\alpha \tag{38}$$

and

$$E_\alpha^{eq} = T\Gamma_\alpha, \tag{39}$$

where $\dot{\gamma}_\alpha$ is the energy source term defined according to the source term in Eq. (3):

$$\dot{\gamma}_\alpha = \xi_\alpha\left[\frac{1}{\rho c_p}\left(\sum_{z=1}^N h_z\omega_z - \dot{Q}_R\right)\right]. \tag{40}$$

Defining $\bar{E}_\alpha = E_\alpha + \frac{E_\alpha - E_\alpha^{eq}}{2\tau_t} - \frac{\delta t}{2}\dot{\gamma}_\alpha$ and integrating Eq. (38) along the characteristics over time step δt, the following LB equation for the temperature field is derived:

$$\bar{E}_\alpha(x_i + e_{\alpha i}\delta t, t + \delta t) = \bar{E}_\alpha(x_i, t) - \frac{\bar{E}_\alpha - \bar{E}_\alpha^{eq}}{\tau_T + 0.5}\bigg|_{(x_i,t)}$$
$$+ \delta t\dot{\gamma}_\alpha\bigg|_{(x_i,t)}, \tag{41}$$

where $\tau_T = \lambda_T/\delta t$ is the nondimensional thermal relaxation time which is related to the thermal diffusivity by $\alpha_{th} = \tau_T c_s^2\delta t$. The nondimensional thermal relaxation time is calculated by $\tau_T = C\tau_{Tl} + (1-C)\tau_{Tg}$ in which τ_{Tl} and τ_{Tg} are the bulk thermal relaxation times for the liquid and gas phases, respectively. They are related to τ_l and τ_g through the Prandtl number for each phase. Taking the zeroth-order moment of the modified energy distribution function gives us the temperature

$$T = \sum_\alpha \bar{E}_\alpha + \frac{\delta t}{2}\dot{\gamma}_\alpha. \tag{42}$$

The rate of evaporation $\dot{m}'''$ in Eqs. (28) and (34) is related to the gradients of temperature and concentration by

$$\dot{m}''' = \frac{K}{h_{fg}}\frac{\partial T}{\partial x_i}\frac{\partial C}{\partial x_i}, \tag{43}$$

where h_{fg} is the latent heat of evaporation of the fuel [20].

D. Lattice Boltzmann equation for the mass fraction of chemical species

The discrete LB equation and its equilibrium distribution function for evolution of the mass fraction of chemical species are [33]

$$\frac{DS_{\alpha z}}{Dt} = \frac{\partial S_{\alpha z}}{\partial t} + e_{\alpha i}\frac{\partial S_{\alpha z}}{\partial x_i} = -\frac{1}{\lambda_{sz}}\left(S_{\alpha z} - S_{\alpha z}^{eq}\right) + \dot{\chi}_\alpha, \tag{44}$$

and

$$S_{\alpha z}^{eq} = Y_z\Gamma_\alpha, \tag{45}$$

in which $\dot{\chi}_\alpha$ is the mass fraction source term, which is defined as

$$\dot{\chi}_\alpha = \xi_\alpha\left(\frac{1}{\rho}\omega_z\right). \tag{46}$$

Introducing $\bar{S}_{\alpha z} = S_{\alpha z} + \frac{S_{\alpha z} - S_{\alpha z}^{eq}}{2\tau_{sz}} - \frac{\delta t}{2}\dot{\chi}_\alpha$ and integrating Eq. (44) along the characteristics over time step δt lead to the following LB equation for chemical species mass fraction:

$$\bar{S}_{\alpha z}(x_i + e_{\alpha i}\delta t, t + \delta t) = \bar{S}_{\alpha z}(x_i, t) - \frac{\bar{S}_{\alpha z} - \bar{S}_{\alpha z}^{eq}}{\tau_{sz} + 0.5}\bigg|_{(x_i,t)}$$
$$+ \delta t\dot{\chi}_\alpha\bigg|_{(x_i,t)}, \tag{47}$$

where $\tau_{sz} = \lambda_{sz}/\delta t$ is the dimensionless relaxation time for the chemical species that is related to the mass diffusivity by $D_z = \tau_{zs}c_s^2\delta t$. The nondimensional mass fraction relaxation times are calculated by $\tau_{sz} = C\tau_{szl} + (1-C)\tau_{szg}$ in which τ_{szl} and τ_{szg} are the bulk thermal relaxation times for species of the liquid and gas phases, respectively. The mass fractions are related to the zeroth-order moment of the modified distribution function for the chemical species according to

$$Y_z = \sum_\alpha \bar{S}_{\alpha z} + \frac{\delta t}{2}\dot{\chi}_\alpha. \tag{48}$$

As mentioned in Sec. II A, the LB equation for the chemical species mass fraction is solved for all the species except for nitrogen, for which it is computed from $\sum_{z=1}^N Y_z = 1$.

E. Solution procedure

The solution algorithm, depicted in Fig. 1, is detailed below:

(1) The macroscopic properties $(u_i, T, Y_z, v, \alpha_{therm}, D_z, \cdots)$ and the corresponding equilibrium distribution functions are initialized according to Eqs. (16), (31), (39), and (45). The initial conditions are applied by setting the distribution functions equal to their equilibrium values.

(2) Equations (28), (34), (41), and (47) are solved without the chemical reaction source terms. There is no need to modify
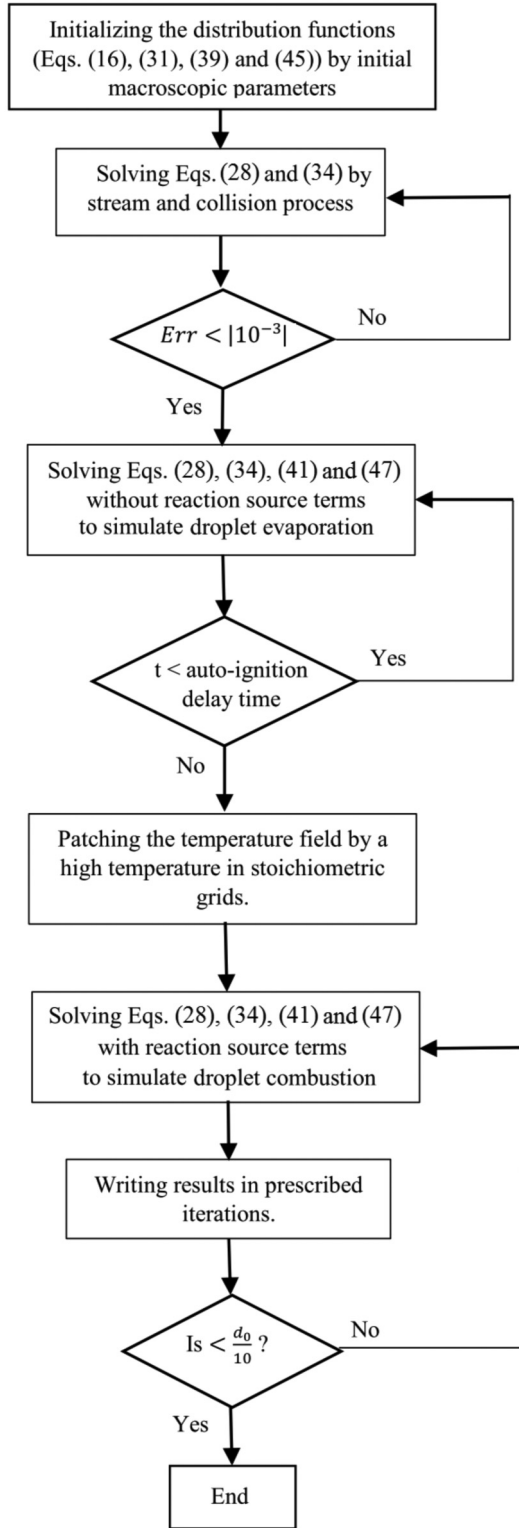
FIG. 1. The flow chart of the solution procedure for combustion.

the relaxation times yet because the variation in temperature and chemical composition is initially negligible. This step, which is used to initiate the evaporation process, is repeated for a predefined time equal to the autoignition delay time [14,15].

(3) The results of the solution in step 2 are used as initial conditions for the combustion simulation. In this step, the source terms in energy and chemical species are calculated in every time step. To activate the combustion reaction, a high temperature is temporarily applied to grids with stoichiometric mass fractions of fuel and oxidizer. The dimensionless relaxation times and the macroscopic properties are updated in every time step as a function of the temperature [14]. The solution procedure is continued until the diameter of the droplet reaches a prescribed threshold.

IV. NUMERICAL RESULTS

To evaluate the proposed LB scheme, the combustion of a stagnant droplet in a quiescent medium in the absence of gravity is studied in detail.

A. Geometry and boundary conditions

Figure 2 shows a schematic of the two-dimensional (2D) domain. To save the computational resources, the simulations are conducted in a quarter of the domain with symmetric boundary condition at the bottom and left. At the right and top boundaries, the outflow boundary condition is applied for $\bar{h}_\alpha$ while the convective boundary condition is used for $\bar{g}_\alpha$. Additionally, the outflow boundary conditions for $\bar{E}_\alpha$ and $\bar{S}_{\alpha z}$ are constant temperature and constant mass fraction, respectively [20]. More details on implementing these boundary conditions are given in the Appendix. The initial conditions are $T_g = T_\infty$, $Y_{O_2} = 0.23$, and $Y_{N_2} = 0.77$ for the gas phase, and $T_l = T_b - 1$ and $Y_{\text{fuel}} = 1.0$ for the liquid phase. Throughout the simulations, the temperature of the fuel droplet is set 1 K below the boiling point T_b to avoid initiation of boiling inside the droplet.

Table I presents the properties of *n*-heptane and *n*-butanol [13,42], which are used as the fuels in our study.
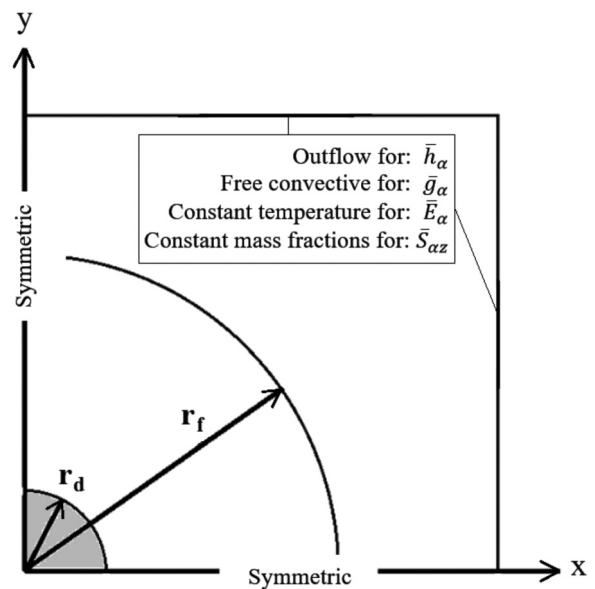

FIG. 2. Schematic of the computational domain. r_d is the radius of the droplet and r_f is the radius of the flame. Detailed explanation on implementing the boundary conditions is given in the Appendix.

TABLE I. Properties of the fuels at boiling point.

Fuel	T_b (K)	ρ (kg/m^3)	h_{fg}(kJ/mol)	h_{comb}(kJ/mol)	K_{ov} (m^3/kmol s)	E(kJ/kmol)	μ (μPa s)
n-Heptane	371	610	36.5	4817	3.35×10^{10}	1.53×10^5	170
n-Butanol	391	730	43	2670			50

The initial diffusion coefficients for the chemical species are $D_{\text{H}_2\text{O}} = 2.2 \times 10^{-5}$(m^2/s), $D_{\text{CO}_2} = 1.6 \times 10^{-5}$(m^2/s), $D_{\text{O}_2} = 2.1 \times 10^{-5}$(m^2/s), $D_{\text{C}_7\text{H}_{16}} = 1.1 \times 10^{-5}$(m^2/s) and $D_{\text{C}_4\text{H}_9\text{OH}} = 1.4 \times 10^{-5}$(m^2/s) [43].

B. Grid independency

First, the grid independency and convergence study of the results is carried out by comparing the d^2 law and the temperature distribution for combustion of an n-heptane droplet with $R_0 = 100 \mu$m on three different grids. The radius of the droplet, R_0, is set to 12, 24, and 48 lattice points, which corresponds to 2D grids with 256, 512, and 1024 grid points in each direction, respectively. Initially, the temperature of the gas phase is $T_\infty = 1200$ K. Figure 3 shows the d^2-law results. As can be seen, there is an excellent match between the d^2-law results for different grids. Figure 4 shows the dimensionless temperature versus the radial distance, which is normalized by the radius of the droplet. Since the spatial distance x is nondimensionalized by the instantaneous droplet radius, the maximum temperature stands for the FSR. As can be seen in Fig. 4, the curves indicate that the results for the temperature profile, flame temperature, and FSR are converged. Figures 3 and 4 confirm the grid independency of the solution in these grid ranges. For the rest of the simulations, the computational domain is discretized using 512×512 grid points and the initial radius of droplet is set to $R_0 = 24 lu$. The domain is chosen large enough to minimize boundary effects.

For the convergence study, the L^2-norm error in calculating the diameter of the droplet at half of its lifespan is computed by:

$$\|\delta_d\| = \sqrt{\frac{(d_{\text{LBM}} - d_{\text{ana}})^2}{d_{\text{ana}}^2}},$$

where d_{LBM} is the droplet diameter obtained from the LB simulations and d_{ana} is the value calculated analytically from the d^2 law for a burning droplet. In Fig. 5, the L^2-norm error is plotted against the number of grid points in the x direction. As can be seen, close to a second-order convergence rate is obtained.

C. Validation of the evaporation model

The results of the d^2 law for evaporation of an n-heptane droplet are validated with both analytical results for constant properties [2] and a benchmark study with variable properties [14]. The initial radius of the droplet in both simulations is $R_0 = 100 \mu$m. The Spalding number, also known as the transfer number, is defined as $B_q = c_{pg}(T_\infty - T_b)/h_{fg}$, and the d^2-law relation is given by

$$\left(\frac{d}{d_0}\right)^2 = 1 - K\frac{t}{d_0^2}, \tag{49}$$

where d_0 is the initial diameter of the droplet and $K = \frac{8k_g}{\rho_l c_{pg}} \ln(1 + B_q) = 0.3147$ is the evaporation constant. Additionally, k_g and c_{pg} are the thermal conductivity and specific heat capacity of the gas, respectively. Note that the units of
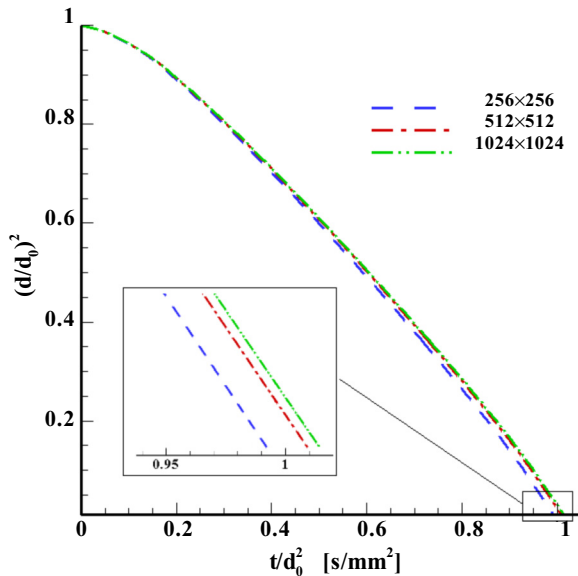

FIG. 3. The d^2-law results for a 100-μm droplet obtained using three different grid resolutions. The square of the drop diameter, which is rescaled by its value at $t = 0$, is plotted versus normalized time (for convenience, time is divided by d_0^2).
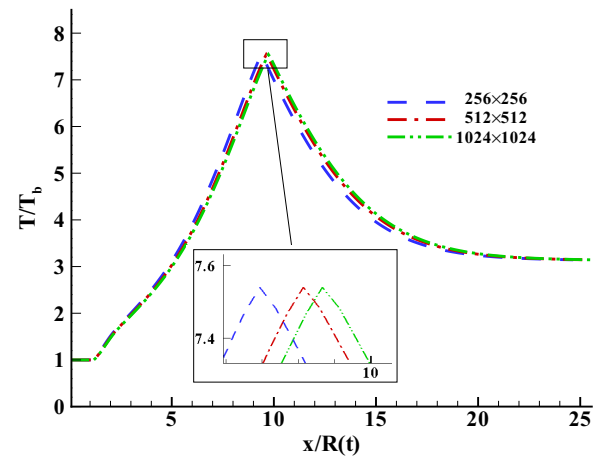

FIG. 4. The temperature profile, rescaled by the boiling point, versus the dimensionless distance, which is measured from the center of the droplet, for three different grids. The distance is nondimensionalized by the instantaneous radius of the droplet so that the location of maximum temperature stands for the flame standoff ratio (FSR).
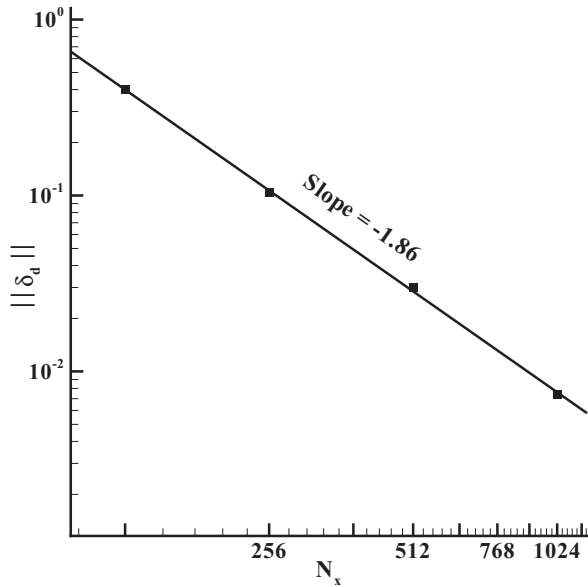
FIG. 5. The L^2-norm error in calculating the droplet diameter versus the number of grid points in the x direction.

diameter in Eq. (49) are millimeters. The properties of the air are evaluated at $\bar{T} = (T_\infty + T_b)/2$ in which $T_\infty = 1200$ K is the ambient air temperature and T_b is the boiling temperature of n-heptane which is given in Table I.

It has been shown that two parameters affect the evaporation process in diffuse-interface models [21]. The first one is the interfacial thickness and the second one is a cutoff value, C_{cutoff}, which determines the approximate location of the droplet radius within the interfacial region. This instantaneous droplet radius is used to calculate the FSR. In all of our simulatioms, the interface thichness is set to 4 lu and the cutoff value is $C_{cutoff} = 0.7$. These values are found to result in the best match between our numerical simulations and experiment data [21]. The rate of change in the diameter of the droplet, which is called the diameter history, obtained from our numerical simulations, is compared with both the analytical solution given in Eq. (49) and the existing numerical results [14]. Figure 6(a) shows good agreement between LBM and analytical results. A comparison between the current LBM and the numerical results using the finite-volume (FV) method [14] is also presented in Fig. 6(b), and, as can be seen, the results for the d^2 law coincide very well. As depicted in Fig. 6, the evaporation rate that is obtained by the proposed LB model is in good agreement with that available analytical (maximum 4% deviation) and numerical data.

D. Validation of the combustion model

To verify the proposed model for combustion, two different cases are considered and compared with available experimental and numerical results [14,15]. As the first case, the combustion of an n-butanol droplet with $d_0 = 0.56$ mm is simulated and the variation of droplet diameter and FSR histories are compared with experimental data in Ref. [15]. The combustion is modeled by an infinitely fast reaction in
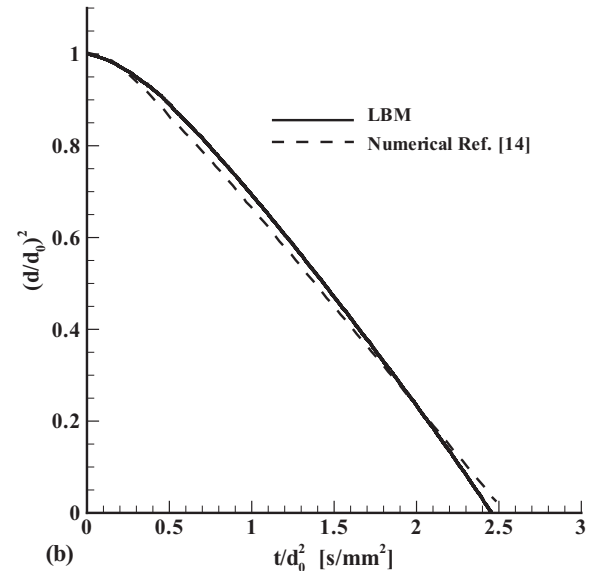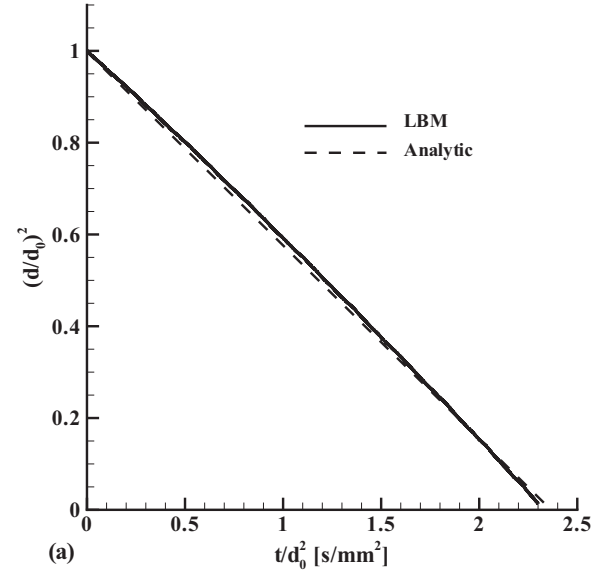

FIG. 6. The diameter histories for evaporation of an n-heptane droplet in quiescent air at 1200 K. Comparison between (a) analytical solution [Eq. (49)]; and (b) finite-volume results [14]. The square of the drop diameter, which is rescaled by its value at $t = 0$, is plotted versus normalized time (for convenience, time is divided by d_0^2).

standard conditions ($T_\infty = 298$ K) according to

$$C_4H_9OH + 6(O_2 + 3.77N_2)$$
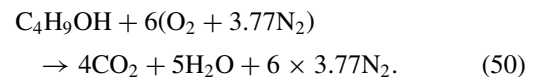$$\rightarrow 4CO_2 + 5H_2O + 6 \times 3.77N_2. \quad (50)$$

Figure 7 presents the results of the current LB model for variation of the droplet diameter and FSR with time together with the experimental data [15]. As can be seen, the diameter history is in good agreement with the experimental data in Fig. 7(a). The FSR results, however, show some deviation from experimental data, particularly at initial times. Figure 7(b) indicates that the present LB model overestimates the initial location of the flame compared to the experimental results. This is partly due to the fact that the relaxation times, which
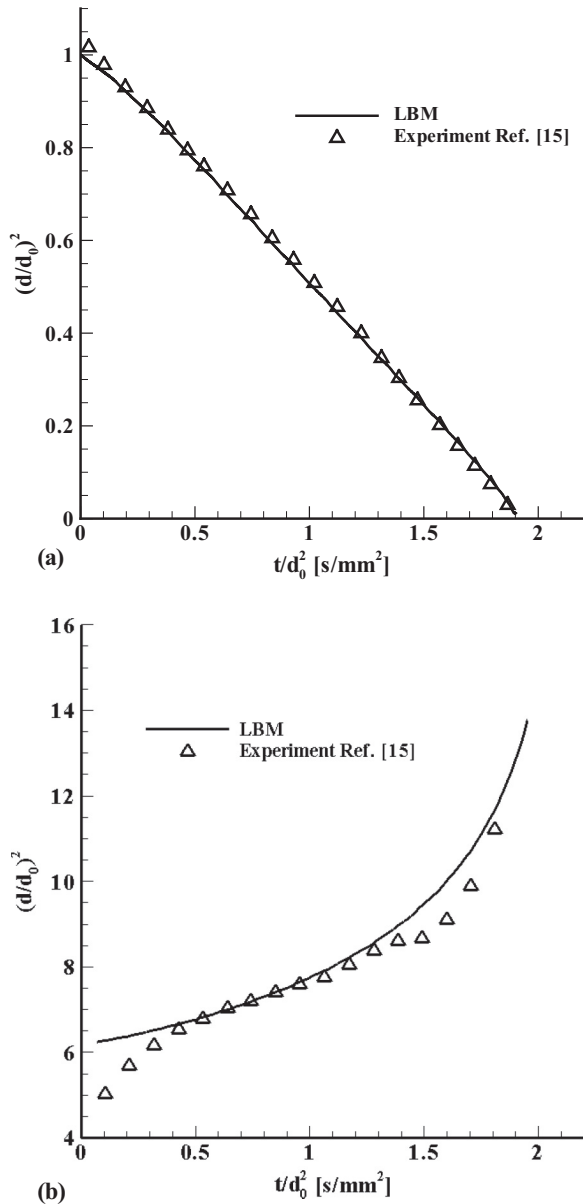
(a)

(b)

FIG. 7. Combustion of an *n*-butanol droplet of diameter 560 μm in ambient air at 298 K. Comparison between the numerical results and the experimental data by Alam *et al.* [15] for (a) the law, and (b) the FSR.

are proportional to the diffusion coefficients, are calculated as a function of the average temperature in the gas phase. This may yield a larger diffusion coefficient near the droplet because the average temperature is above the local temperature. As a result, the vapor fuel diffuses faster such that the initial location of the flame is predicted to be farther away than that in the experiments. In the late stages of the droplet combustion, the grid resolution around the shrinking droplet might not be sufficient. This may lead to very sharp gradients across the interface of the droplet, which in turn diminishes the numerical accuracy. This is potentially responsible for deviation of our results from experimental data. Therefore, it is anticipated that using adaptive mesh refinement (AMR) techniques will
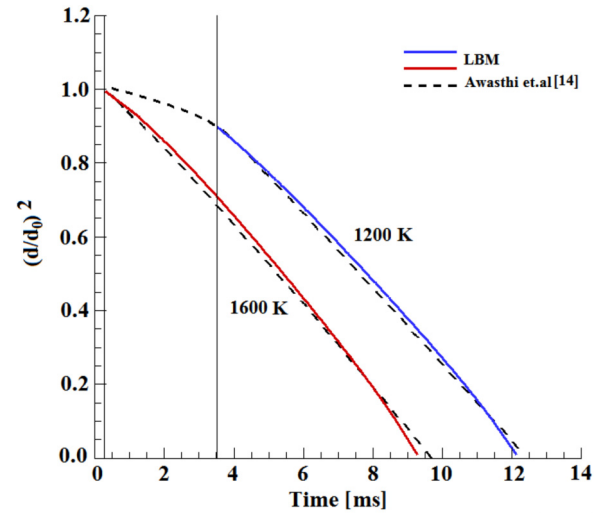

FIG. 8. Combustion of *n*-heptane droplets of diamater 100 μm in ambient air at 1200 and 1600 K. The square of the droplet diameter, which is rescaled by its initial value at $t = 0$, is plotted versus time.

improve the accuracy, as well as efficiency, of the simulations, particularly at late times [44,45].

As the second test case, the combustion of an *n*-heptane droplet is studied and the results are compared with the numerical results by Awasthi *et al.* [14]. The combustion is modeled by an overall single-step reaction according to

$$C_7H_{16} + 11(O_2 + 3.77N_2) \rightarrow 7CO_2 + 8H_2O + 11 \times 3.77N_2.$$

$$(51)$$
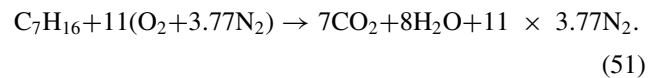
Heptane droplets burn with a sooty yellow flame when the diameter is larger than about 70 μm [46]; the soot formation involves luminous heat loss. In both Awasthi *et al.* [14] and the present study, the soot formation and its heat loss are ignored. The simulations performed by Awasthi *et al.* [14] included autoignition, extinction, and burnout, while these phenomena are not considered in the present LB model. In our simulations, the ignition is modeled by applying a temporary high temperature to the grids with stoichiometric mass fractions of fuel and oxygen at predefined autoignition delay times given in Ref. [14]. The simulations are stopped once the diameter of the droplet reaches one-tenth of the initial diameter.

We place a droplet with $d_0 = 100$ μm in ambient air at $T = 1200$ K and $T = 1600$ K. Figure 8 represents a comparison between the droplet diameter histories obtained by the current LBM and the CFD simulations for combustion of an *n*-heptane droplet. The vertical lines show the autoignition delay times in Awasthi *et al.* [14], which are $t = 3.48$ ms for $T = 1200$ K and $t = 0.25$ ms for $T = 1600$ K. The curves show good agreement between LBM and CFD results for the diameter histories.

Figure 9 shows the FSR results for the combustion of the *n*-heptane droplet in the ambient air at $T = 1200$ K and $T = 1600$ K. The ignition delay times are excluded from the curves of Awasthi *et al.* [14]. The transient nature of autoignition affects both the shape of the curve and the initial location of the flame [47], as is evident in the FSR curves. Although
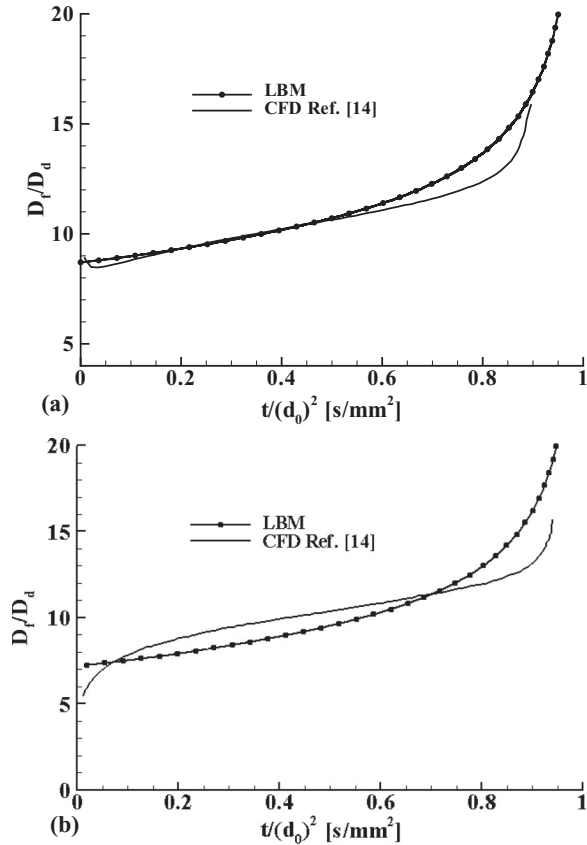
FIG. 9. The FSR for combustion of an n-heptane droplet of diameter 100 μm in ambient air at (a) 1200 K, and (b) 1600 K.

the diffusion coefficients at 1200 K are smaller than those at 1600 K, the bigger delay time for combustion at 1200 K causes a bigger initial FSR in both simulations. The LBM results show some deviations at higher ambient temperatures and at later stages of the combustion. As explained earlier, we suspect that using the average temperature for calculation of the relaxation times could be responsible for these deviations. Nevertheless, the proposed LB formulation has an acceptable accuracy in a wide range of droplet lifetime.

Figure 10 shows the variation of the dimensionless temperature along the radial direction for the combustion occurring at an ambient air temperature of 1200 K with time. It should be mentioned that, in order to obtain comparable curves, the spatial distance x must be nondimensionalized by the instantaneous radius of droplet R rather than the initial radius R_0. Hence, the location where the temperature is maximum can be considered as the FSR. The maximum temperature (between 2800 and 2870 K) shows good agreement with that reported by Awasthi *et al.* [14].

Figure 11 shows the mass fraction of the chemical species along the radial direction. Since the spatial distance x is nondimensionalized by the instantaneous radius, the location of the flame, where the fuel mass fraction is zero, gives us the FSR. The curves show that the LB scheme calculates the mass fractions correctly because the sum of mass fractions at any radial distance is equal to 1, as expected.
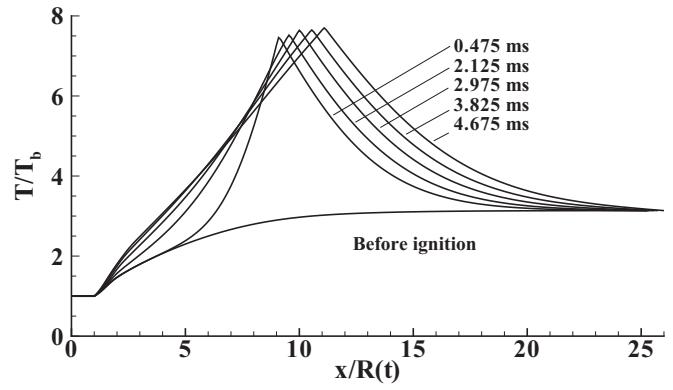

FIG. 10. The dimensionless temperature profile at different times ($T_b = 371$ K). The x distance is nondimensionalized by instantaneous droplet radius so that the x location where the temperature is maximum stands for the FSR.
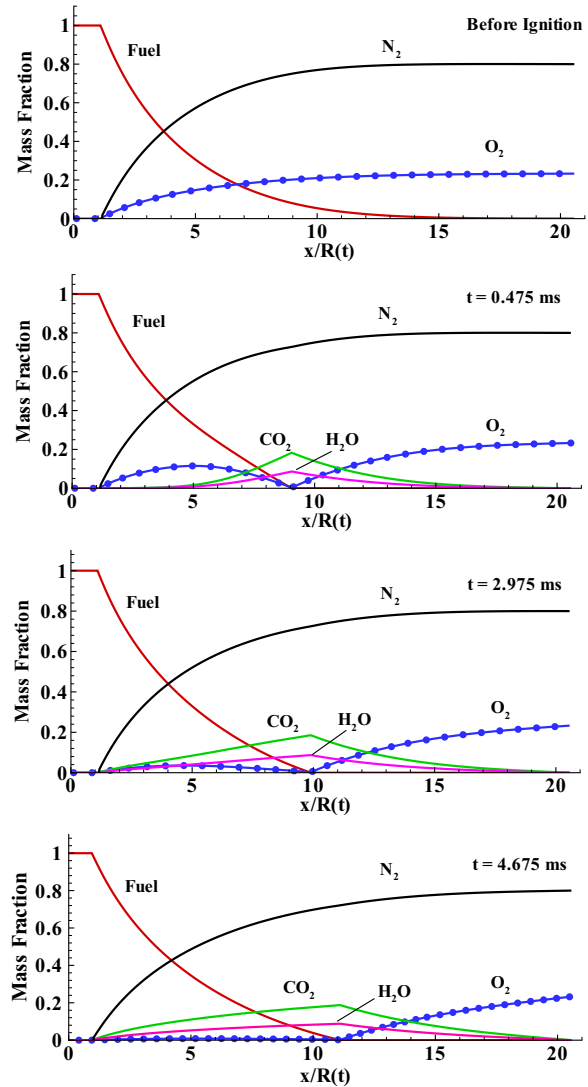

FIG. 11. Mass fraction profiles at different times. The x distance is nondimensionalized by the instantaneous droplet radius so that the location where the fuel mass fraction is zero stands for the FSR.
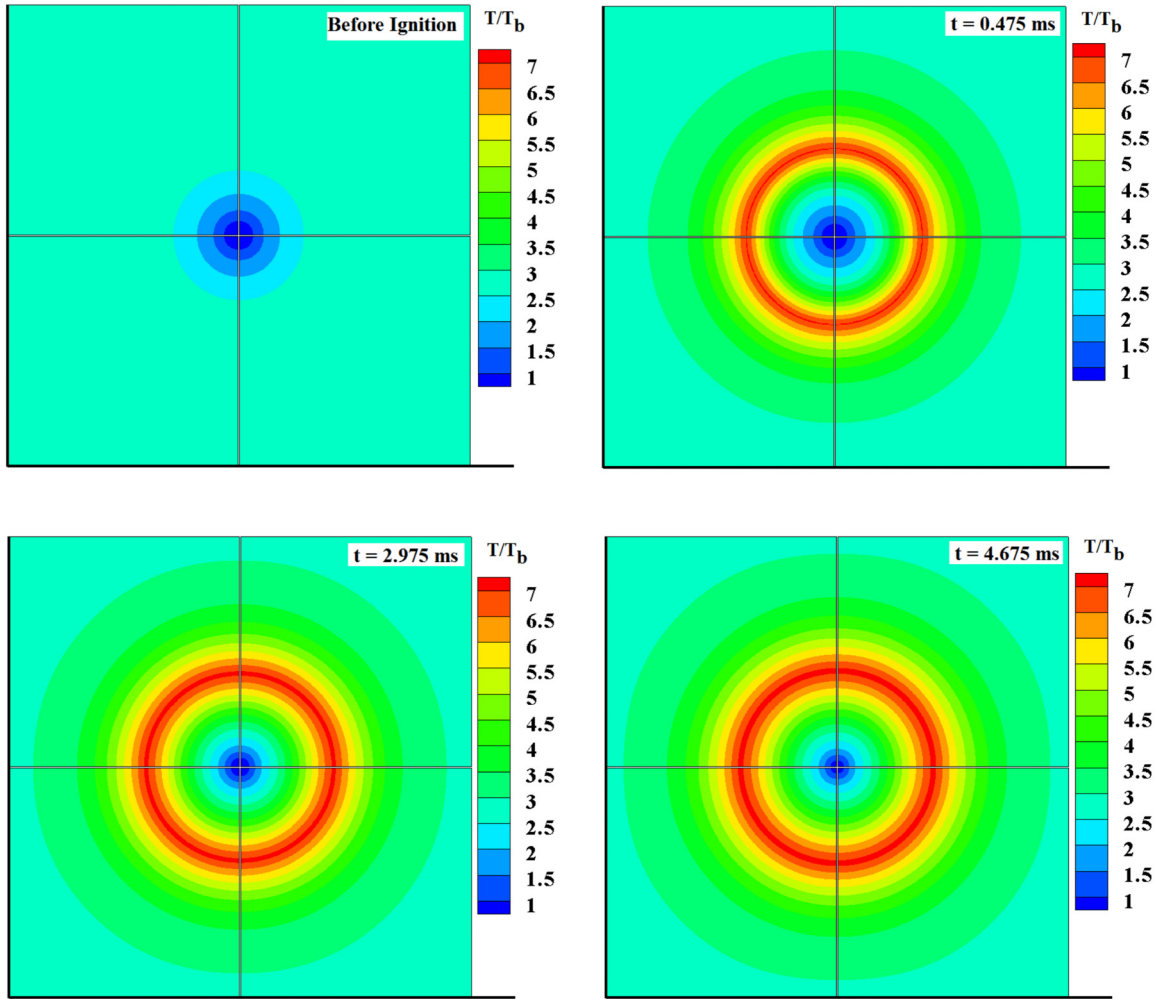
FIG. 12. Dimensionless temperature contours at different times during combustion. The flame radius, shown by maximum temperature, increases until it reaches a maximum value, after which it remains nearly constant.

Figure 12 presents contour plots of temperature at four different times. The contours of maximum temperature represent the location of the flame. The flame radius increases until it reaches a maximum radius, after which it remains nearly constant. Therefore, after this stage, the increase in the FSR is mainly due to the decrease in the droplet radius.

As mentioned in the Introduction, the weakness of the majority of previous LB simulations of combustion is the constant-density approach, which leads to an underestimation in calculating the velocity field. Here, to show this, we consider a constant-density system, in which the gas density is a function of the chemical composition only and does not change with temperature. Figure 13 presents a comparison between the density contours for constant-density and variable-density solutions. In Fig. 13(a), the value of the density decreases from the initial liquid density to the initial gas density, while in the variable-density approach in Fig. 13(b) the density decreases below the initial gas density in the flame zone. This reduction in the density, which is due to the rise of temperature in the flame zone, causes an increase in the velocity field between the droplet and the flame. This increase in the velocity field is shown in Fig. 14.

Figure 14 shows the dimensionless velocity profile across the symmetric boundary (the x axis). The velocity is normalized by the Stefan velocity, which is defined as the bulk velocity of evaporation, at the interface. Figure 14 shows that the velocity magnitude is larger than the Stefan velocity farther away from the droplet in the variable-density approach. In the constant-density approach, the velocity decreases along the radius at a rate inversely proportional to the radius (in 2D) to satisfy the continuity equation; i.e., $\boldsymbol{u} \cdot \boldsymbol{A} = $ const. In the variable-density approach $\rho \boldsymbol{u} \cdot \boldsymbol{A} = $ const.; therefore the velocity is inversely proportional to ρr, and the larger the radius the smaller the density. In other words, the velocity increases beyond the Stefan velocity outside the interface until it reaches a maximum value. There is a slight fluctuation in the flame zone caused by variations in the chemical composition. Figure 14 also shows that using the constant-density approach leads to a smaller FSR, which causes a higher evaporation rate and a shorter droplet lifetime.
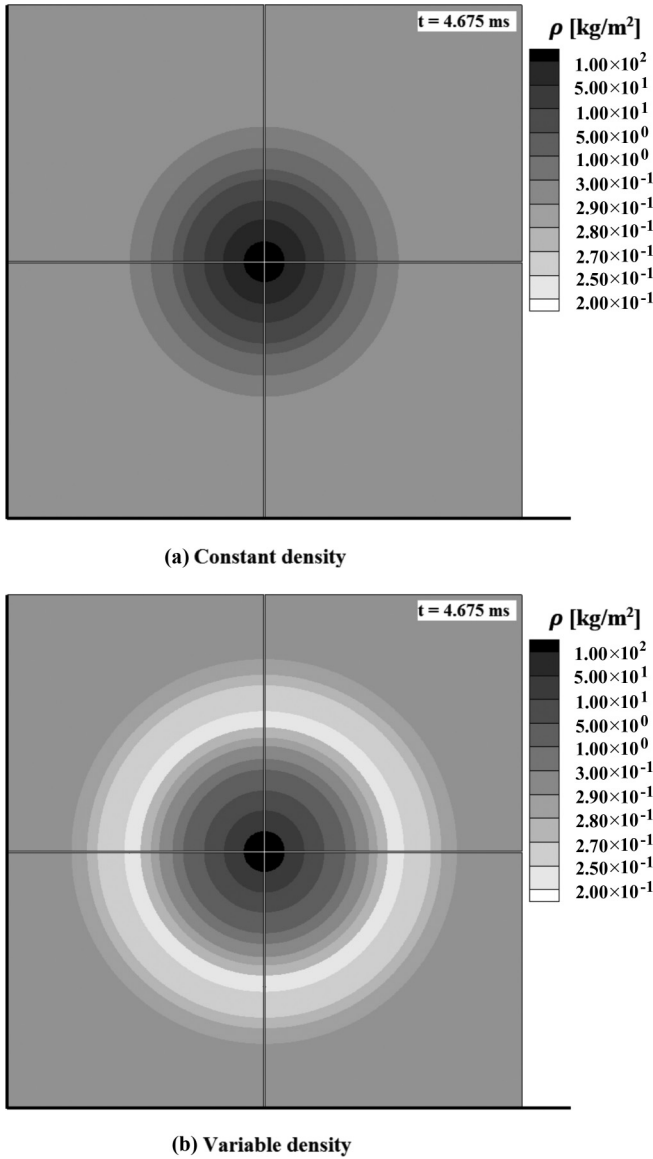
(a) **Constant density**

(b) **Variable density**

FIG. 13. Contours of density. Comparison between (a) constant-density, and (b) variable-density approaches.
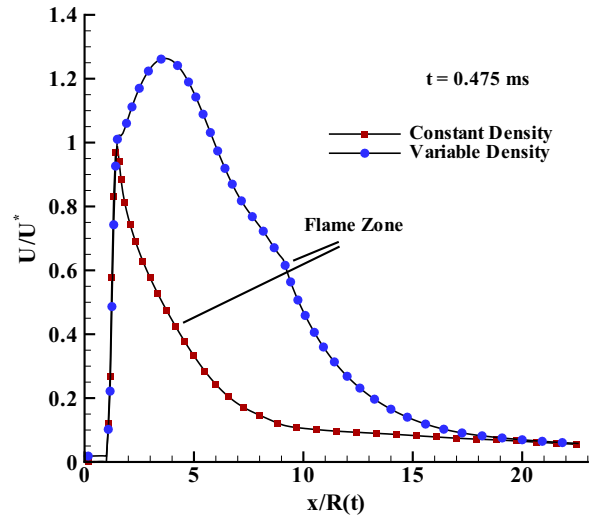

FIG. 14. A comparison between dimensionless velocity profiles for constant-density and variable-density approaches. The velocity is rescaled by the Stefan velocity (which is defined as the bulk velocity of evaporation, at the interface). In the variable-density approach, the velocity increases beyond the Stefan velocity outside the interface.

V. SUMMARY AND FUTURE WORK

A Cahn-Hilliard-based lattice Boltzmann scheme was formulated for simulation of droplet combustion in this study. The proposed LB model accounts for some important features, such as density variation, chemical species variation, nonluminous heat radiation, and variable Lewis and Prandtl numbers, all of which were neglected in previous studies. Our variable-density model was shown to give more realistic results mainly because it can predict the correct velocity profile by accounting for the density variation between the flame and the droplet. The diameter history predicted by the proposed model was found to be in close agreement with CFD-based simulations [14]. On the other hand, the FSR results showed some deviation from CFD simulations and experiments, especially at late stages of droplet lifetime when the ambient temperature is high. We suspect the following reasons to be responsible for this deviation, and we suggest remedies for each, which will outline the direction of our future work:

I. Our model does not include the autoignition process. To consider the autoignition process, the combustion must be modeled by a more detailed chemical kinetic scheme that involves elementary reaction steps with the chain-initiation and chain-propagating reactions [48].

II. We assumed the relaxation times are functions of the mean temperature. Using the local temperature, instead of the mean temperature, to update the relaxation times leads to more accurate diffusion coefficients, particularly in the flame zone.

III. The grid resolution might not be enough at the late stages of combustion, where the droplet has shrunk significantly, leading to inaccurate calculation of the gradient terms. Using AMR techniques [44,45] can improve the accuracy of the results, especially at late times.

The proposed model can handle large density ratios up to 1000, which is typical for an air-fuel system. For the density ratio of 1000, the proposed model is capable of simulating droplet combustion with initial kinematic viscosity ratios up to $v_g/v_l = 18$. Although our LB model for combustion is proposed and tested in 2D, its extension to 3D is straightforward and will be considered in our future studies.

APPENDIX

In this Appendix, we describe the initial and boundary conditions used in our simulations.

1. Initial conditions

In the case of a stationary droplet, we set the initial velocity and pressure to zero, and the order parameter is initialized according to the following hyperbolic tangent profile:

$$C(r) = \frac{1}{2} + \frac{1}{2} \tanh\left(\frac{2r}{\epsilon}\right), \tag{A1}$$

where r is the distance from the center of the droplet. The density is interpolated according to Eq. (8). Then the distribution functions are set to their equilibrium values using Eqs. (16), (31), (39), and (45).

2. Boundary conditions

For the distribution function that is used for interface tracking, the unknown, incoming components at the outflow boundary, $\boldsymbol{x}_b$, are computed by a linear extrapolation:

$$\bar{h}_\alpha(\boldsymbol{x}_b,t) = 2\bar{h}_\alpha(\boldsymbol{x}_b - \boldsymbol{e}_\alpha \delta t,t) - \bar{h}_\alpha(\boldsymbol{x}_b - 2\boldsymbol{e}_\alpha \delta t,t). \quad \text{(A2)}$$

For the hydrodynamic distribution function, the convective boundary condition is used at the outflow boundary, $\boldsymbol{x}_b$, for the incoming components according to

$$\frac{\partial \bar{g}_\alpha}{\partial t} + u_i \cdot \frac{\bar{g}_\alpha}{\partial x_i} = 0, \quad \text{(A3)}$$

which yields the following formula after temporal and spatial discretization using the explicit Euler scheme,

$$\bar{g}_\alpha(x_{ib},t) = \frac{\bar{g}_\alpha(x_{ib},t-\delta t) + \bar{g}_\alpha(x_{ib} - e_{i\alpha}\delta t,t)\theta_i}{1+\theta_i}, \quad \text{(A4)}$$

where $\theta_i = u_i(x_{ib},t-\delta t)\delta t/\delta x$. After finding the unknown components of $\bar{h}_\alpha$ and $\bar{g}_\alpha$ at the boundaries, the order parameter

(and hence the density) and the velocity at the outlet can be computed using Eqs. (35), (8), and (36).

For implementing the boundary conditions for the temperature and the mass fraction of chemical species, we first calculate the auxiliary parameter Γ_α according to Eq. (17). In the approach proposed by Inamuro *et al.* [49], which is used in this study, it is assumed that the energy distribution function can be approximated by its equilibrium value at an unknown temperature T' (to be specified shortly). Therefore, the unknown components of the distribution function at the boundaries are approximated according to

$$\bar{E}_\alpha(T) = \bar{E}_\alpha^{eq}(T') = T'\Gamma_\alpha. \quad \text{(A5)}$$

The unknown temperature T' is determined so that the desired value for the temperature at the boundary, T_{bound}, is obtained. In other words,

$$\sum_\alpha \bar{E}_\alpha = \sum_{\text{unknown}} T'\Gamma_\alpha + \sum_{\text{known}} \bar{E}_\alpha = T_{\text{bound}}. \quad \text{(A6)}$$

After we determine T' from Eq. (A6), the unknown components of the energy distribution function are computed using Eq. (A5). The constant mass fraction boundary condition can be implemented, similarly.

[1] International Energy Agency (2015), http://www.worldenergyoutlook.org/weo2015/.

[2] S. R. Turns, *An Introduction to Combustion: Concepts and Applications*, 3rd ed. (McGraw-Hill, New York, 2012).

[3] G. M. Faeth, Symp. (Int.) Combust. [Proc.] **26**, 1593 (1996).

[4] C. K. Law, Prog. Energy Combust. Sci. **8**, 171 (1982).

[5] G. A. E. Godsave, Symp Combust. **4**, 818 (1953).

[6] H. H. Chiu, Prog. Energy Combust. Sci. **26**, 381 (2000).

[7] W. A. Sirignano, *Fluid Dynamics and Transport of Droplets and Sprays*, 2nd ed. (Cambridge University Press, Cambridge, 1999).

[8] S. Ulzama and E. Specht, Proc. Combust. Inst. **31**, 2301 (2007).

[9] W. A. Sirignano, Prog. Energy Combust. Sci. **42**, 54 (2014).

[10] V. V. Tyurenkova, Acta Astronaut. **75**, 78 (2012).

[11] G. Wu and W. A. Sirignano, Combust. Flame **157**, 970 (2010).

[12] T. I. Farouk, Y. C. Liu, A. J. Savas, C. T. Avedisian, and F. L. Dryer, Proc. Combust. Inst. **34**, 1609 (2013).

[13] I. Awasthi, G. Gogos, and T. Sundararajan, Combust. Flame **160**, 1789 (2013).

[14] I. Awasthi, D. N. Pope, and G. Gogos, Combust. Flame **161**, 1883 (2014).

[15] F. E. Alam, Y. C. Liu, C. T. Avedisian, F. L. Dryer, and T. I. Farouk, Proc. Combust. Inst. **35**, 1693 (2015).

[16] X. He and L.-S. Luo, Phys. Rev. E **56**, 6811 (1997).

[17] X. He and G. D. Doolen, J. Stat. Phys. **107**, 309 (2002).

[18] A. Fakhari and M. H. Rahimian, Phys. Rev. E **81**, 036707 (2010).

[19] A. Fakhari and T. Lee, Phys. Rev. E **87**, 023304 (2013).

[20] H. Safari, M. H. Rahimian, and M. Krafczyk, Phys. Rev. E **88**, 013304 (2013).

[21] H. Safari, M. H. Rahimian, and M. Krafczyk, Phys. Rev. E **90**, 033305 (2014).

[22] A. Begmohammadi, M. Farhadzadeh, and M. H. Rahimian, Int. Commun. Heat Mass Transfer. **61**, 78 (2015).

[23] A. Begmohammadi, M. H. Rahimian, M. Farhadzadeh, and M. A. Hatani, Comput. Math. Appl. **71**, 1861 (2016).

[24] S. G. Ayodele, F. Varnik, and D. Raabe, Phys. Rev. E **83**, 016702 (2011).

[25] S. Succi, G. Bella, and F. Papetti, J. Sci. Comput. **12**, 395 (1997).

[26] T. Poinsot and D. Veynante, *Theoretical and Numerical Combustion* (R. T. Edwards Inc., Philadelphia, 2001).

[27] O. Filippova and D. Haenel, Comput. Phys. Commun. **129**, 267 (2000).

[28] O. Filippova and D. Hänel, Int. J. Mod. Phys. C **9**, 1439 (1998).

[29] O. Filippova and D. Hänel, J. Comput. Phys. **158**, 139 (2000).

[30] K. Yamamoto, X. He, and G. D. Doolen, J. Stat. Phys. **107**, 367 (2002).

[31] K. Yamamoto, JSME Int. J. **47**, 403 (2004).

[32] T. Lee, C.-L. Lin, and L.-D. Chen, J. Comput. Phys. **215**, 133 (2006).

[33] S. Chen, Z. Liu, C. Zhang, Z. He, Z. Tian, B. Shi, and C. Zheng, Appl. Math. Comput. **193**, 266 (2007).

[34] S. Chen, Z. Liu, Z. Tian, B. Shi, and C. Zheng, Comput. Math. Appl. **55**, 1424 (2008).

[35] T. Lee, Comput. Math. Appl. **58**, 987 (2009).

[36] N. Latifiyan, M. Farhadzadeh, P. Hana, and M. H. Rahimian, Int. Commun. Heat Mass Transfer **71**, 56 (2016).

[37] M. A. Hatani, M. Farhadzadeh, and M. H. Rahimian, Int. Commun. Heat Mass Transfer **66**, 218 (2015).

[38] R. S. Barlow, A. N. Karpetis, J. H. Frank, and J. Y. Chen, Combust. Flame **127**, 2102 (2001).

[39] H. Ding, P. D. M. Spelt, and C. Shu, J. Comput. Phys. **226**, 2078 (2007).

[40] T. Lee and L. Liu, J. Comput. Phys. **229**, 8045 (2010).

[41] X. He, S. Chen, and G. D. Doolen, J. Comput. Phys. **146**, 282 (1998).

[42] D. N. Pope and G. Gogos, Combust. Flame **142**, 89 (2005).

[43] K. Khalid, R. A. Khan, S. Mohd. Zain, P. Pemalar, T. Pengakti-fan, and O. Terpilih, in *Proceedings of International Conference on Bangladesh Environment Network, Dhaka, Bangladesh*, Vol. 41, (2012), p. 1109.

[44] A. Fakhari and T. Lee, Phys. Rev. E **89**, 033310 (2014).

[45] A. Fakhari, M. Geier, and T. Lee, J. Comput. Phys. **315**, 434 (2016).

[46] H. Hara and S. Kumagai, Symp. (Int.) Combust., [Proc.] **25**, 423 (1994).

[47] S. K. Aggarwal, Prog. Energy Combust. Sci. **45**, 79 (2014).

[48] S. Soylu and J. Van Gerpen, Fuel **82**, 1699 (2003).

[49] T. Inamuro, M. Yoshino, H. Inoue, R. Mizuno, and F. Ogino, J. Comput. Phys. **179**, 201 (2002).